Nanoscale

Accepted Manuscript

This article can be cited before page numbers have been issued, to do this please use: W. Zhao, X. Zhou, D. Yan, Y. Huang, C. Li, Q. Gao, P. Moras, P. M. Sheverdyaeva, H. Rong, Y. Cai, E. F. Schwier, X. Zhang, C. Shen, Y. Wang, Y. Xu, W. Ji, C. Liu, Y. Shi, L. Zhao, L. Bao, Q. Wang, K. Shimada, X. Tao, G. Zhang, H. Gao, Z. Xu, X. Zhou and G. Liu, *Nanoscale*, 2025, DOI: 10.1039/D4NR05191B.

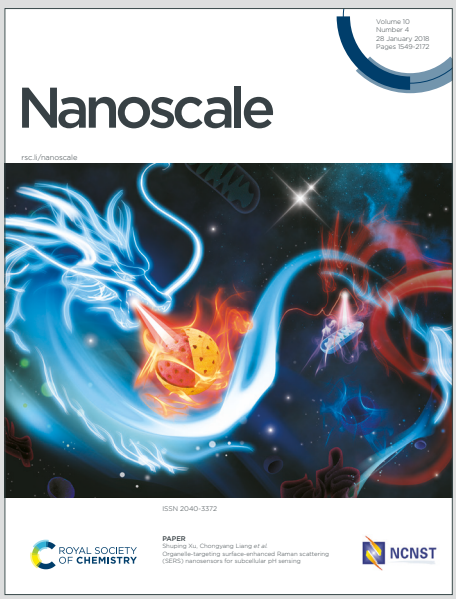

ROYAL SOCIETY OF CHEMISTRY

rsc.li/nanoscale

View Article Online
DOI: 10.1039/D4NR05191B

View Article Online
DOI: 10.1039/D4NR05191B

Journal Name

ARTICLE TYPE

Cite this: DOI: 00.0000/xxxxxxxxxx

Synthesis and Electronic Structure of Atomically Thin 2H-$MoTe_2$†

Wenjuan Zhao, [a,b,c,*‡] Xieyu Zhou, [d‡] Dayu Yan, [a,b‡] Yuan Huang, [a,e,*] Cong Li, [a,b] Qiang Gao, [a,b] Paolo Moras, [c] Polina M. Sheverdyaeva, [c] Hongtao Rong, [a,b] Yongqing Cai,[a,b] Eike F. Schwier, [f] Xixia Zhang,[g] Cheng Shen, [a,b] Yang Wang, [a,b] Yu Xu, [a,b] Wei Ji, [d] Chen Liu, [h] Youguo Shi, [a] Lin Zhao, [a] Lihong Bao, [a] Qingyan Wang, [a] Kenya Shimada, [f] Xutang Tao, [g] Guangyu Zhang, [a,b] Hongjun Gao, [a,b] Zuyan Xu, [i] Xingjiang Zhou, [a,b,j,k,*] Guodong Liu [a,b,j,*]

Received Date
Accepted Date

DOI: 00.0000/xxxxxxxxxx

An in-depth understanding of the electronic structure of 2H-$MoTe_2$ at the atomic layer limit is a crucial step towards its exploitation in nanoscale devices. Here, we show that millimeter-sized monolayer (ML) $MoTe_2$ samples, as well as smaller sized bilayer (BL) samples, can be obtained using the mechanical exfoliation technique. The electronic structure of these materials is investigated by Angle-Resolved Photoemission Spectroscopy (ARPES) for the first time and Density Functional Theory (DFT) calculations. The comparison between experiments and theory allows us to describe ML $MoTe_2$ as a semiconductor with direct gap at K point. This scenario is reinforced by the experimental observation of the conduction band minimum at K in Rb-doped ML $MoTe_2$, resulting in a gap of at least 0.924 eV. In the BL $MoTe_2$ system the maxima of the bands at Γ and K display very similar energies, thus leaving the door open to a direct gap scenario, in analogy to WSe_2. The monotonic increase in the separation between spin-split bands at K while moving from ML to BL and bulk-like $MoTe_2$ is attributed to interlayer coupling. Our findings can be considered as a reference to understand Quantum Anomalous and Fractional Quantum Anomalous Hall Effects recently discovered in ML and BL $MoTe_2$ based moiré heterostructures.

0.1 Introduction

Monolayer transition metal di-chalcogenides (TMDCs) with the formula MX_2 (where M = Mo, W; X = S, Se, Te) and 2H phase

[a]Beijing National Laboratory for Condensed Matter Physics, Institute of Physics, Chinese Academy of Sciences, Beijing 100190, China
[b]University of Chinese Academy of Sciences, Beijing 100049, China
[c]CNR-Istituto di Struttura della Materia (CNR-ISM), SS 14, Km 163,5, 34149 Trieste, Italy
[d]Department of Physics, Renmin University of China, Beijing 100872, P.R. China
[e]School of Physics, School of Integrated Circuits and Electronics, Beijing Institute of Technology, Advanced Research Institute of Multidisciplinary Sciences, Beijing 100081, China;
[f]Hiroshima Synchrotron Radiation Center, Hiroshima University, Higashi-Hiroshima, Hiroshima 739-0046, Japan
[g]State Key Laboratory of Crystal Materials, Shandong University, 250100, Jinan, Shandong, China
[h] Institute of High Energy Physics, CAS, 19B Yuquan Road, Shijingshan District, Beijing, China
[i]Technical Institute of Physics and Chemistry, Chinese Academy of Sciences, Beijing 100190, China
[j]Songshan Lake Materials Laboratory, Dongguan, Guangdong 523808, China
[k]Beijing Academy of Quantum Information Sciences, Beijing 100193, China
[‡]These people contributed equally to the present work.
[*]Corresponding authors: Wenjuan.Zhao@trieste.ism.cnr.it (Wenjuan Zhao) yhuang01@iphy.ac.cn (Yuan Huang) XJZhou@iphy.ac.cn (Xingjiang Zhou) gdliu_arpes@iphy.ac.cn(Guodong Liu)

† Supplementary Information available: [details of any supplementary information

View Article Online
DOI: 10.1039/D4NR05191B

exhibit unique and remarkable properties, including direct band gap transition[1–4], well-defined valley degrees of freedom and spin-valley locking[5], huge exciton binding energy[6,7], and Ising superconductivity[8]. Their unique properties can lead to numerous applications in next-generation nanoelectronics[9], optoelectronics[10], and valleytronics[7].

$MoTe_2$ is a small gap semiconductor hosting exotic and prominent quantum phenomena in the few layer limit[11–13]. Recently, the Quantum Anomalous Hall effect (QAH, also mentioned as integer Chern insulating state) has been reported in twisted bilayer (BL) $MoTe_2$[13] and in AB-stacked $MoTe_2$ /WSe_2 moir*é* hetero-BLs[12]. The long-sought-after Fractional Quantum Anomalous Hall Effects (FQAH, also called fractional Chern insulating state) has been discovered only in twisted BL $MoTe_2$[13–16], although it had been predicted in some twisted TMDC moir*é* BLs[12,17–19]. Thus, the rhombohedral-stacked twisted $MoTe_2$-based BLs have emerged as a promising platform for investigating both QAH and FQAH effects at zero magnetic field. Additionally, a giant intrinsic spin Hall effect has also been found in AB-stacked $MoTe_2$/WSe_2 moir*é* BLs[20–22]. These findings open the way to investigate novel physical properties such as fractional charge excitation and anyon statistics under zero magnetic field conditions, thus providing new opportunities for dissipationless transport, topological quantum computing and spintronics[13–16,20,23]. In spite of the importance of $MoTe_2$, there have been no reports on the electronic band structures of monolayer (ML) $MoTe_2$, which is the ultimate building block of the moir*é* hetero-structures mentioned above.

Compared to the Molecular Beam Epitaxy growth method[24], mechanical exfoliation is a simpler and more universal technique. It typically results in weaker substrate interactions and yields higher quality samples[25]. In this paper, we report on the synthesis of millimeter-sized ML $MoTe_2$ samples via the mechanical exfoliation method. The superior structural uniformity of the so-obtained layers allows us to perform detailed characterization of their properties by space-averaging techniques, such as Low-Energy Electron Diffraction (LEED), Raman spectroscopy and, for the first time, Angle-Resolved Photoemission Spectroscopy (ARPES). The electronic structure of ML $MoTe_2$ displays a flat state around Γ and valence band maximum (VBM) at the K point, which are closely reproduced by Density Functional Theory (DFT) calculations. On the basis of this agreement, the system can be described as a semiconductor with direct gap at K point. The observation of conduction band filling at K in Rb-doped ML $MoTe_2$ strengthens this scenario. Occasionally, mechanical exfoliation gives rise to well-ordered patches of BL $MoTe_2$ surrounded by areas of ML and multilayer (bulk-like) $MoTe_2$. The topmost occupied states at Γ and K in these BLs display similar binding energy. This may suggest that BL $MoTe_2$ is a direct gap semiconductor, in analogy to BL WSe_2[26]. Finally, we discover that the energy separation of the spin-split states at K increases monotonically from ML to BL and to multilayer $MoTe_2$ as a consequence of the interlayer coupling. Our work sheds light on the electronic structure of atomically thin $MoTe_2$ layers, thus providing fundamental support to understand the origin of QAH and FQAH effects occurring in $MoTe_2$-based hetero-structures.

available should be included here]. See DOI: 00.0000/00000000.

0.2 Methods

ML, BL and multilayer (bulk-like) $MoTe_2$ flakes were prepared by the mechanical exfoliation method from bulk crystals, as illustrated in Fig. 1(a)[25]. ARPES measurements on ML and multilayer (more than 10 MLs) samples were performed with photon energy of 21.218 eV, using a home-build photoemission spectroscopy system[27] equipped with a VUV5000 Helium lamp (spot size 0.8 mm × 0.8 mm) and a DA30L electron energy analyzer (Scienta Omicron). The overall energy resolution was set to 20 meV, and the angular resolution to 0.2°. ARPES data of BL samples were collected at the BL-1 end station of the Hiroshima Synchrotron Radiation Center (HiSOR) with photon energy of 45 eV (spot size 0.8 mm × 0.3 mm). All the samples were measured at 30 - 40K in a base pressure better than 5×10^{-11} mbar, after mild vacuum annealing at about 500 K.

DFT calculations were performed using the generalized gradient approximation and the projector augmented wave method[28,29] as implemented in the Vienna ab-initio simulation package (VASP)[30,31]. A uniform Monkhorst-Pack k mesh of 21×21×5 was adopted for integration over the Brillouin zone of bulk $MoTe_2$, and a mesh of 21×21×1 for ML and BL $MoTe_2$. A plane-wave cutoff energy of 700 eV was used for structural relaxation and electronic structures. A distance of more than 15 $\mathring{A}$ along out-of-plane direction was adopted to eliminate interaction between adjacent layers. Dispersion correction was made at the van der Waals Density Functional (vdW-DF) approach[32–34], with the optB86b functional for the exchange potential, which was proved to be accurate in describing the structural properties of layered materials[35–40] and was adopted for structure related calculations. All atoms were allowed to relax until the residual force per atom was less than 0.01 eV/$\mathring{A}$. In our electronic structure calculation, we used the Perdew-Burke-Ernzerhof (PBE)[41] function with consideration of spin-orbit coupling (SOC), based on the vdW-DF optimized atomic structures. A plane-wave cutoff energy of 500 eV and a k mesh of 9×9×3 were used for energy calculations for bulk $MoTe_2$ (9×9×1 for ML and BL).

0.3 Results and Discussion

Fig. 1(a) illustrates the sample preparation procedure of atomically-thin $MoTe_2$ samples by the mechanical exfoliation method[25]. The SiO_2/Si substrate (black rectangle) is cleaned by oxygen plasma, covered with a 3-20 nm thick layer of gold (yellow rectangle) and cleaned again by oxygen plasma and ultrasonication. An adhesive tape (blue rectangle) loaded with bulk $MoTe_2$ layer (green rectangle) is brought into contact with the substrate and then removed to complete the exfoliation process. Fig. 1(b-e) reports the characterization of samples prepared according to this procedure. Typically, optical microscope images (Fig. 1(b)) reveal the presence of millimeter-sized $MoTe_2$ domains (pink areas) covering most of the substrate (dark pink areas). After mild annealing (500 K) in ultra-high vacuum conditions, a sharp hexagonal LEED pattern becomes visible (Fig.

View Article Online
DOI: 10.1039/D4NR05191B

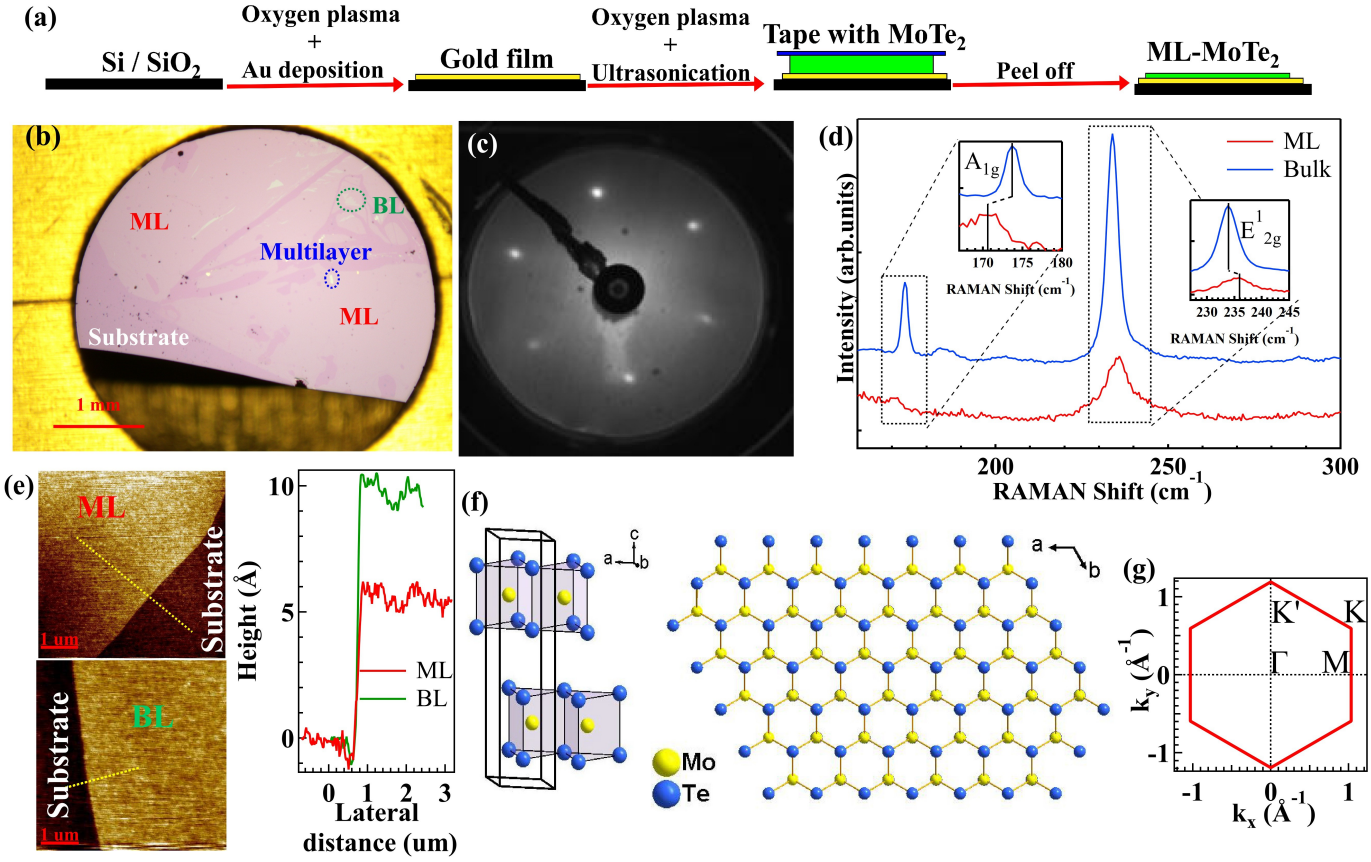

Fig. 1 (a) Cartoon illustrating the sample fabrication process. Black, yellow, green, and blue rectangular bars represent the SiO_2/Si wafer, gold film, $MoTe_2$ layer, and adhesive tape, respectively. (b) Typical optical microscope image of a sample after mechanical exfoliation of $MoTe_2$. The predominant pink areas are millimeter-sized domains of ML $MoTe_2$ in contact with the substrate (dark pink areas). Small light pink and white areas surrounded by dotted ovals represent BL and multilayer $MoTe_2$, respectively. (c) LEED pattern taken on a sample with prevalent ML $MoTe_2$ coverage. (d) Raman spectra of ML (red) and bulk (blue) $MoTe_2$. Characteristic peaks are highlighted in the insets. (e) AFM images taken at the edge between the Au substrate and ML (top panel) and BL (bottom panel) $MoTe_2$ domains. The thickness profiles extracted from the lines shown in the AFM images are compared in the right panel. (f) Crystal structure of $MoTe_2$ in isometric and top views. (g) SBZ of $MoTe_2$.

1(c)), thus indicating the long-range order of the $MoTe_2$ domains. In order to determine the vibrational properties of these domains, Fig. 1(d) compares the Raman data acquired on the pink area of Fig. 1(b) (red spectrum) and on bulk-like (more than 10 MLs) $MoTe_2$ (blue spectrum) with a laser wavelength of 532 nm. In the blue spectrum the A_{1g} mode is located at 173.67 cm^{-1} and the E^1_{2g} mode at 233.87 cm^{-1}, while in the red spectrum they are found at 170.58 cm^{-1} and 235.92 cm^{-1}, respectively (insets in Fig. 1(d)). These shifts from the reference bulk-like values are consistent with previously reported results for ML $MoTe_2$ [42]. The topmost atomic force microscopy (AFM) image in Fig. 1(e) shows directly that the height difference between the substrate and the millimeter-sized $MoTe_2$ domains is 5.97 $\pm$ 1 $\mathring{A}$ (red line in the right panel), which is in the range of the expected thickness of ML $MoTe_2$ (6.98 $\mathring{A}$). Overall, these experimental data allow us to identify the pink areas of Fig. 1(b) as well-ordered domains of ML $MoTe_2$.

Fig. 1(b) displays also small regions (typical size in the order of 0.1 mm) with light pink and white optical contrast. The AFM analysis of the light pink areas (bottommost image in Fig. 1(e)) shows that their height with respect to the substrate corresponds to 10.32 $\pm$ 1 $\mathring{A}$, i.e. nearly twice the measured thickness of ML $MoTe_2$. Therefore, these areas are identified as domains of BL $MoTe_2$. Finally, the white areas are bulk-like multilayers of $MoTe_2$. Occasionally, the mechanical exfoliation method produces millimeter sized area of BL and multilayer (from here onwards called bulk) $MoTe_2$, which allow space-averaging ARPES analysis, as it will be shown in Fig. 2. Fig. S1 of the Supplemental Material [43] shows the structural characterization of a sample with BL domains in the order of 1 mm^2, where the thickness of the BL areas is measured by AFM and confirmed by cross-sectional transmission electron microscopy.

For reference, Fig. 1(f) displays the crystal structure of 2H-$MoTe_2$, which comprises van der Waals Te-Mo-Te trilayers (left panel) stacked along the c-axis and forming a honeycomb lattice in the (0001) projection plane (right panel). The prisms of adjacent trilayers point in opposite directions within the plane. Among the TMDCs, $MoTe_2$ possesses notably large lattice parameters (a = 3.52 $\mathring{A}$, c = 13.97 $\mathring{A}$) [44]. Fig. 1 (g) presents the surface Brillouin zone (SBZ) of $MoTe_2$, along with high symmetry points,

View Article Online
DOI: 10.1039/D4NR05191B

which will be useful for the discussion of the ARPES data.

Fig. 2 reports an overview of the ARPES analysis along the M-Γ-K-M path for ML (Fig. 2(a,d)), BL (Fig. 2(b,e)) taken on a millimeter sized domain of the sample shown in Fig. S1 and bulk (Fig. 2(c,f)) $MoTe_2$. The spectra are shown as acquired in the top row and after second derivative treatment (along the energy axis) in the bottom row, to enhance the sensitivity to weak electronic features. The well-defined Fermi level (E_F) observed in the second derivative data derives from the partially uncovered Au layer in the substrate. The calculated band structures (red dotted lines) are overlaid to the data in the bottom row of the figure (see Fig. S2 of the Supplemental Material for calculations extended above E_F [43]).

In the ML sample (Fig. 2(a, d)), the topmost band observed near Γ is very flat and mainly derives from Mo d_{z2} orbitals, with minor Te p_z contribution, which exhibit significant localization in the lattice plane (calculations of the orbital character are reported in Fig. S3 of the Supplemental Material[43]). The two parabolic-like bands with maxima at the K point primarily derive from in-plane delocalized Mo d_{x2-y2}/d_{xy} orbitals, with small contribution from Te p_x/p_y orbitals. These bands form a spin-split pair, originating from the strong SOC of Mo atoms and the absence of structural inversion symmetry, and become degenerate along the Γ-M direction due to time-reversal symmetry. The VBM is found at K (-0.76 eV), which lies well above the topmost state at Γ (-1.375 eV) (see also Fig. S4 of the Supplemental Material). The observations of a flat band at Γ and of VBM at K are consistent with other ML-MX_2 materials[26,45–47]. In addition to these characteristic features, two parabolic bands centered at the M point with energies ∼ -1.25 eV and -1.7 eV, as well as another parabolic band centered at the Γ point around -2 eV, are discernible. The increasing background below -2 eV in Fig. 2(a,d) originates from the intense 5d states of the underlying polycrystalline gold substrate. The experimental band structure of the ML $MoTe_2$ sample within the first 2 eV below E_F turns out to be well reproduced by the calculations (Fig. 2(d)). This good correspondence allows us to describe ML $MoTe_2$ as a direct band gap semiconductor.

Figure 3 presents further data supporting the direct band gap scenario in ML $MoTe_2$. To determine directly the momentum position of the conduction band minimum (CBM), Rb atoms are evaporated on the surface of ML $MoTe_2$ to partially fill its unoccupied bands[48]. The changes induced by Rb deposition in the band structure of ML $MoTe_2$ along the Γ-K direction are shown in Fig. 3(a-d). With increasing the amount of deposited Rb, the bands shift continuously away from E_F (Fig. 3(b-d)). At the highest Rb coverage (Fig. 3(d)) the VBM and the topmost state at Γ are located at -0.96 and -1.66 eV. The detailed evolution of the bands at the Γ and K points is depicted through the energy distribution curves (EDCs) taken at the $k_{||}$ positions marked by the orange dashed lines in Fig. 3(a) and illustrated in Fig. 3(e) and (f), respectively. These EDCs demonstrate a peak shift of 0.285 eV at the Γ point and 0.2 eV at the K point. These data indicate a non-rigid band shift that could be used for electronic structure engineering of ML $MoTe_2$.

Interestingly, the spectra acquired in the proximity of K' (cut 2 in the inset of Fig. 3(a)) for the highest Rb deposition display a peak near E_F (inset in Fig. 3(g)). The emergence of this feature can be followed in Fig. 3(h), which shows the EDCs extracted at K' for both pristine (red) and highly Rb doped $MoTe_2$ (green). The peak is identified as the CBM at the K' point. Together with the VBM at K/K' point, this new state proves the existence of a direct gap of at least 0.924 eV. This gap value is different from that of pristine $MoTe_2$ because of band renormalization effects, which clearly manifest in the non-rigid Rb-induced band shifts. However, it is close to the gap size expected from the DFT calculation (0.97 eV, Fig S3). This observation is in line with other band calculations[43,49,50], photoluminescence[49,51,52] and STS[24] measurements for ML $MoTe_2$.

BL and bulk $MoTe_2$ exhibit electronic bands similar to those of the ML case with differences mainly concentrated around the Γ point. In Fig. 2(b, e), an additional parabolic band is present above the flat band. In Fig. 2(c, f), a complex packed structure of parabolic bands is observed above the flat band, which is consistent with the reported results for more than 3 ML thick $MoTe_2$ samples[11,48]. The orbital calculation in Fig. S3[43] indicates that the parabolic band (BL) and packet of bands (bulk) can be explained by the repulsion between Mo d_{z2} and Te p_z orbitals perpendicular to the plane. This repulsion increases the energy at Γ in BL and bulk $MoTe_2$ and reduces the energy from Γ to M and Γ to K because of the increasing component of in-plane orbitals. Below the flat band, the parabolic bands become clearer in BL and bulk $MoTe_2$ samples.

It's worth noting that the topmost valence states of BL $MoTe_2$ at both Γ and K are located at -0.795 eV (a detailed comparison is provided in Fig. S5 of the Supplemental Material[43]). This situation is analogous to that observed in BL WSe_2, which is predicted to be a direct gap semiconductor[26,53,54], but contrasts with most indirect-gap BL TMDC semiconductors, such as MoS_2, WS_2, and $MoSe_2$, where the VBM is found at Γ[45,53,55–57]. Our ARPES data may suggest the presence of a direct gap at K in BL $MoTe_2$, which would be consistent with the results of low-temperature photoluminescence experiments[51,58,59]. However, our calculations (Fig. S2[43]) reveal that the CBM is located half-way between Γ and K. This inconsistency can be attributed to the slight lattice mismatch between the calculated freestanding BL and the real BL $MoTe_2$ on the Au substrate, which was not considered in our calculations[60,61]. ARPES is inherently unable to directly observe the conduction band due to the lack of electron occupation, thus precluding the verification of the CBM position through this method. Further investigation is required to clarify the nature (direct vs indirect gap semiconductor) of BL $MoTe_2$.

For bulk $MoTe_2$, the topmost valence state at the Γ point (-0.665 eV) is closer to E_F than that at K (-0.87 eV), thus indicating a typical indirect gap semiconductor behavior. Overall, the valence band structures in Fig.2 provide clear evidence for the indirect-to-direct band gap transition with decreasing the layer thickness from bulk (indirect gap) to ML (direct gap). This transition originates from the quantum confinement effect[2,62] and is consistent with the reported photoluminescence results[49,51,52,63].

The splitting of the valence bands (VB1 and VB2) near the K point holds significance for various crucial phenomena and properties of MX_2 materials, including spin-valley locking, AB exciton

View Article Online
DOI: 10.1039/D4NR05191B

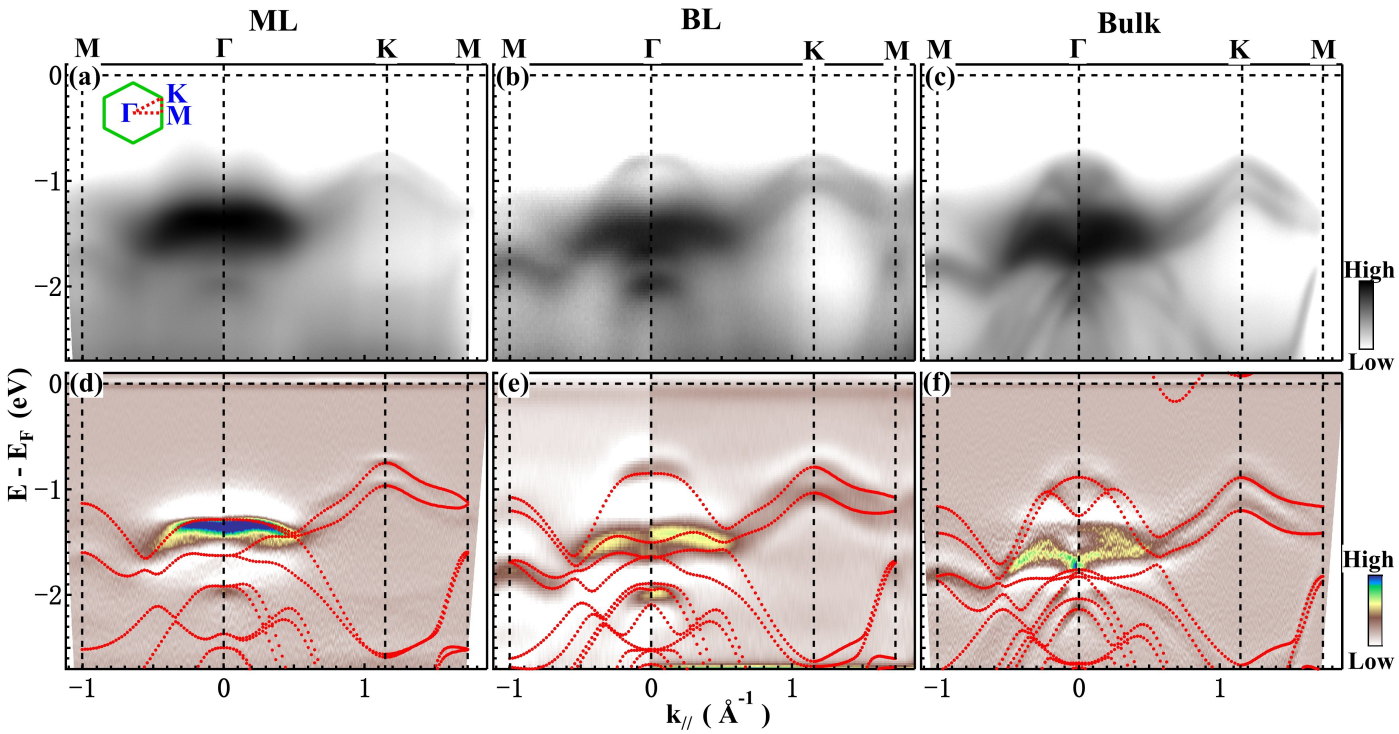

Fig. 2 (a - c) ARPES maps illustrating the electronic band structures along the M-Γ-K-M high symmetry direction in ML (a), BL (b), and bulk (c) $MoTe_2$, as indicated at the top. The inset in (a) shows the high symmetry directions (red dashed lines) in the SBZ (green hexagon). The lower panels (d - f) depict the second derivative plots of panels (a - c), respectively. The red dotted curves overlaid on the plots represent the corresponding bands calculated by DFT.

effect[6,7], and spin-layer locking[64]. In Fig. 4, we show ARPES data along the Γ-K direction for ML, BL and bulk samples (Fig. 4(a-c)) and the corresponding second derivative plots (Fig. 4(d-f)). To facilitate a quantitative comparison, Fig. 4(g-i) display EDCs at the K point for the different samples. The measured splitting at K increases monotonously with thickness (details of the Gaussian fitting are given in Fig. S6[43]): 0.212 eV in ML, 0.225 eV in BL and 0.252 eV in bulk $MoTe_2$. These data are consistent with the trend of the DFT results, which give 0.22, 0.24, and 0.310 eV for the respective systems. Generally, in the family of MX_2 TMDCs, the valence band splitting around the K point arises from SOC, inversion symmetry breaking, and interlayer coupling[5]. The increasing splitting size can be attributed to a variation of the interlayer coupling strengths between BL or bulk (Fig. S7[43]) and ML $MoTe_2$[5,65]. Therefore, our observations imply an interlayer interaction strength in the order of 10 meV and 40 meV for BL and bulk $MoTe_2$, respectively. The increased interlayer coupling strength from BL to bulk is likely to be a consequence of the reduced layer separation as the number of layers increases, thereby enhancing interlayer hopping and coupling[65].

The splitting of spin-polarized bands is a distinctive feature of ML-TMDCs, resulting from the interplay of SOC and the breaking of inversion symmetry[5,66,67]. The splitting in ML $MoSe_2$ is ~ 0.18 eV[45] and in ML MoS_2 is ~ 0.15 eV[46]. The larger splitting which we observed in ML $MoTe_2$ is a consequence of the larger SOC of Te with respect to Se and S. This characteristic makes ML $MoTe_2$ particularly well-suited for applications in spintronics.

To summarize our results in a quantitative way, we have compiled Table 1 with the relevant parameters of the band structures for the different $MoTe_2$ systems derived from ARPES measurements and DFT calculations. Regarding the K splitting, the difference between the VBM at the K and Γ points, and the size of the direct band gap in ML $MoTe_2$, our calculations show consistent results with the ARPES measurements as discussed above. We have also derived the effective mass near the VBM at both K and Γ points along the Γ-K direction (details in Table S1[43]). While going from ML to BL and bulk, the observed effective mass at K shows similar values for the different layered samples. Conversely, at Γ, both the observed and calculated hole effective masses for the top of the valence band exhibit a rapid and monotonic decrease with increasing the number of layers. The discrepancy between the experimental (13.09 m_0) and calculated (34.52 m_0) effective masses at the Γ point for ML $MoTe_2$ primarily arises from hybridization between the $MoTe_2$ and Au states. Our DFT calculations were performed for free-standing $MoTe_2$ layers. Therefore, the interaction with the substrate is not taken into account. The effective mass of the Au sp states (<1 electron mass[68]) is much lower than that of ML $MoTe_2$. As a result of the $MoTe_2$-Au interaction the measured effective mass is lower than the calculated one. A similar effect has been reported in the case of ML MoS_2[69]. Importantly, all ARPES analysis and DFT calculations are consistent.

View Article Online
DOI: 10.1039/D4NR05191B

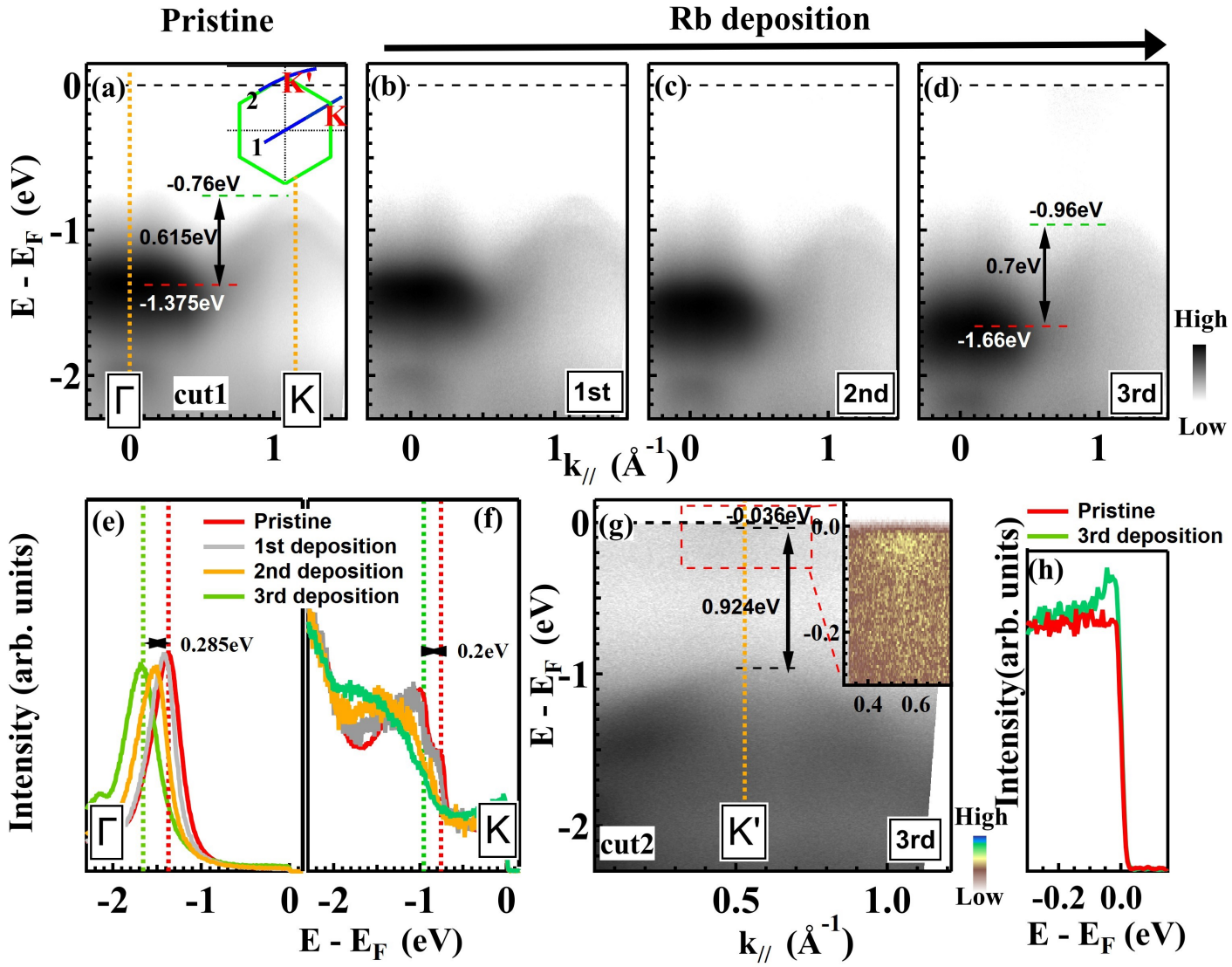

Fig. 3 Direct band gap observation in ML $MoTe_2$ through Rb deposition. ARPES data of (a) pristine and (b-d) Rb-doped $MoTe_2$ ML are measured along cut 1 (Γ-K direction) as shown in the inset of panel (a). Panels (e,f) show the EDCs at the Γ and K points extracted from panels (a-d), respectively. The red and green dashed lines mark the position of the band maxima for the pristine $MoTe_2$ sample and after the 3rd Rb deposition. Panel (g) shows ARPES data along cut2 after the 3rd Rb deposition, where a new band appears near E_F at K' (see inset). Panel (h) shows the EDCs at K' for the pristine $MoTe_2$ (red) and after the 3rd Rb deposition (green).

Table 1 Electronic parameters extracted from ARPES data and DFT calculations of ML, BL and bulk $MoTe_2$. The asterisk (*) indicates the value extracted from the ML sample after Rb deposition. m_0 is the electron mass.

Thickness	ML		BL		Bulk	
	ARPES	Calculation	ARPES	Calculation	ARPES	Calculation
Splitting at K [eV]	0.212	0.22	0.225	0.24	0.252	0.31
Energy difference between VBM at K and Γ [eV]	0.615	0.536	0	0.059	-0.205	-0.005
Gap size [eV]	0.924*	0.97	–	0.91	–	0.72
Effective Mass at K [m_0]	1.17	0.59	1.69	0.62	1.56	0.61
Effective Mass at Γ [m_0]	13.09	34.52	5	8.5	–	1.27

Conclusions

In summary, we report on the synthesis of millimeter-sized ML $MoTe_2$ domains using the mechanical exfoliation method. The exceptional structural uniformity of these layers allows for a comprehensive characterization using space-averaging techniques. Our investigation reveals that the electronic structure of ML $MoTe_2$ features a flat band around the Γ point and a VBM at the K point, in agreement with DFT calculations. This strongly suggests that the material can be described as a semiconductor with a direct band gap at K. The observation of conduction band filling at K

View Article Online
DOI: 10.1039/D4NR05191B

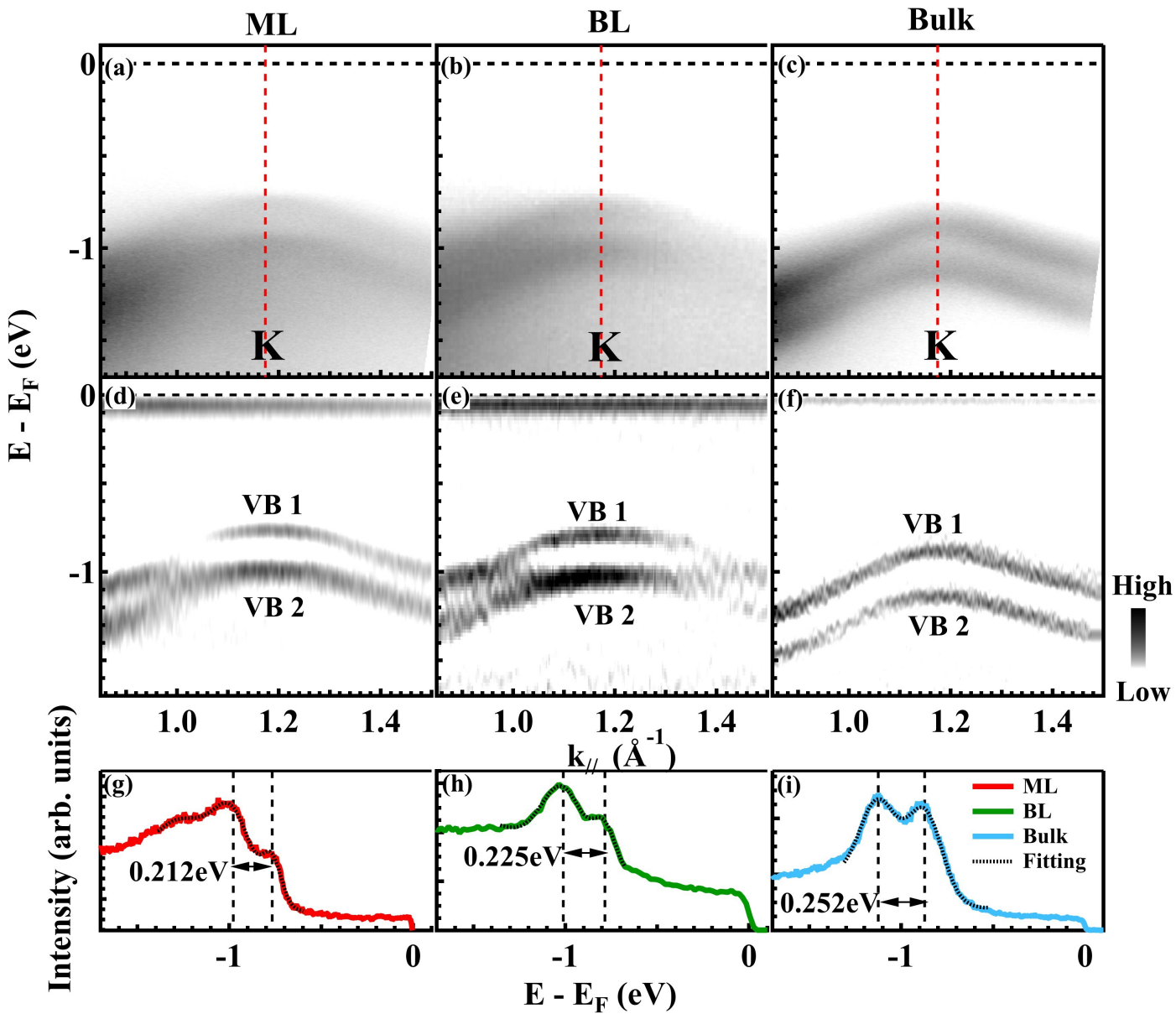

Fig. 4 Layer dependent band splitting at K. (a-c) ARPES maps showing the valence band splitting around K along the Γ-K-M direction for ML, BL and bulk $MoTe_2$, respectively. (d-f) Second derivative spectra of (a-c) along the energy axis, respectively. (g-i) EDCs at K from (a-c), shown as red (ML), green (BL) and blue (bulk) curves, respectively. The black dotted curves are the corresponding Gaussian fitting result, with peak positions indicated by black dashed lines.

in Rb-doped ML $MoTe_2$, with direct band gap of at least 0.924 eV, further support this interpretation. The topmost occupied states of BL $MoTe_2$ at Γ and K exhibit similar binding energies. This opens the possibility that BL $MoTe_2$ is a direct gap system, akin to WSe_2. Finally, the energy separation of the spin-split bands at K increases monotonically from ML to BL to bulk $MoTe_2$ due to interlayer coupling. The present work sheds light on the electronic structure of atomically thin $MoTe_2$ layers, which could be significant to clarify the origin of quantum anomalous Hall (QAH) and fractional quantum anomalous Hall (FQAH) effects observed in $MoTe_2$-based heterostructures.

Author contributions

W.Z., Xie.Z. and D.Y. contributed equally to this work. G.L., Xin.Z. and W.Z. conceptualized the work; W.Z., Q.G., H.R., E. F. S., Y. W., L.Z., K.S. and G.L. conducted the ARPES experiments; C. L., Y.C., Y.X., L.B. and Z.X. provided instrumental support for the ARPES measurements; W.Z., G.L., P.M. and P.M.S. wrote the article with contributions from all coauthors; D.Y., Y.H., Xix.Z., C.S.,C.L.,Y.S.,Q.W., X.T., G.Z., H.G. prepared the samples and performed the Raman, AFM and XPS measurements; Xie. Z. and W.J. conducted the DFT calculations; Y.H., G.L. and Xin.Z. supported the network. W.Z., Y.H., Xin.Z. and G.L. are corresponding authors.

View Article Online
DOI: 10.1039/D4NR05191B

Conflicts of interest

There are no conflicts to declare.

Data availability

The data supporting this article have been included as part of the Supplementary Information [43].

Acknowledgements

This work is supported by the National Key Research and Development Program of China (Nos. 2022YFA1403901, 2019YFA0308000 and 2018YFA0704201), the National Science Foundation of China (Nos. 11574367 and 11874405), and the Youth Innovation Promotion Association of CAS (Nos. 2017013 and 2019007). PM and PMS acknowledge partial funding through the project EUROFEL-ROADMAP ESFRI of the Italian Ministry of University and Research.

References

1 J. K. Ellis, M. J. Lucero and G. E. Scuseria, *Applied Physics Letters*, 2011, **99**, year.
2 Z. Y. Zhu, Y. C. Cheng and U. Schwingenschlögl, *Physical Review B*, 2011, **84**, 153402.
3 T. Cheiwchanchamnangij and W. R. L. Lambrecht, *Physical Review B*, 2012, **85**, 205302.
4 A. Kumar and P. K. Ahluwalia, *The European Physical Journal B*, 2012, **85**, 186.
5 D. Xiao, G.-B. Liu, W. Feng, X. Xu and W. Yao, *Physical Review Letters*, 2012, **108**, 196802.
6 M. M. Ugeda, A. J. Bradley, S.-F. Shi, F. H. da Jornada, Y. Zhang, D. Y. Qiu, W. Ruan, S.-K. Mo, Z. Hussain, Z.-X. Shen, F. Wang, S. G. Louie and M. F. Crommie, *Nature Materials*, 2014, **13**, 1091–1095.
7 J. R. Schaibley, H. Yu, G. Clark, P. Rivera, J. S. Ross, K. L. Seyler, W. Yao and X. Xu, *Nature Reviews Materials*, 2016, **1**, 16055.
8 J. M. Lu, O. Zheliuk, I. Leermakers, N. F. Q. Yuan, U. Zeitler, K. T. Law and J. T. Ye, *Science*, 2015, **350**, 1353–1357.
9 B. Radisavljevic, A. Radenovic, J. Brivio, V. Giacometti and A. Kis, *Nature Nanotechnology*, 2011, **6**, 147–150.
10 S. Manzeli, D. Ovchinnikov, D. Pasquier, O. V. Yazyev and A. Kis, *Nature Reviews Materials*, 2017, **2**, 17033.
11 H. Zhang, C. Bao, Z. Jiang, K. Zhang, H. Li, C. Chen, J. Avila, Y. Wu, W. Duan, M. C. Asensio and S. Zhou, *Nano Letters*, 2018, **18**, 4664–4668.
12 T. Li, S. Jiang, B. Shen, Y. Zhang, L. Li, Z. Tao, T. Devakul, K. Watanabe, T. Taniguchi, L. Fu, J. Shan and K. F. Mak, *Nature*, 2021, **600**, 641–646.
13 H. Park, J. Cai, E. Anderson, Y. Zhang, J. Zhu, X. Liu, C. Wang, W. Holtzmann, C. Hu, Z. Liu, T. Taniguchi, K. Watanabe, J.-H. Chu, T. Cao, L. Fu, W. Yao, C.-Z. Chang, D. Cobden, D. Xiao and X. Xu, *Nature*, 2023, **622**, 74–79.
14 Y. Zeng, Z. Xia, K. Kang, J. Zhu, P. Knüppel, C. Vaswani, K. Watanabe, T. Taniguchi, K. F. Mak and J. Shan, *Nature*, 2023, **622**, 69–73.
15 J. Cai, E. Anderson, C. Wang, X. Zhang, X. Liu, W. Holtzmann, Y. Zhang, F. Fan, T. Taniguchi, K. Watanabe, Y. Ran, T. Cao, L. Fu, D. Xiao, W. Yao and X. Xu, *Nature*, 2023, **622**, 63–68.
16 F. Xu, Z. Sun, T. Jia, C. Liu, C. Xu, C. Li, Y. Gu, K. Watanabe, T. Taniguchi, B. Tong *et al.*, *Physical Review X*, 2023, **13**, 031037.
17 F. Wu, T. Lovorn, E. Tutuc, I. Martin and A. H. MacDonald, *Phys. Rev. Lett.*, 2019, **122**, 086402.
18 T. Devakul, V. Crépel, Y. Zhang and L. Fu, *Nature Communications*, 2021, **12**, 6730.
19 V. Crépel and L. Fu, *Phys. Rev. B*, 2023, **107**, L201109.
20 Z. Tao, B. Shen, W. Zhao, N. C. Hu, T. Li, S. Jiang, L. Li, K. Watanabe, T. Taniguchi, A. H. MacDonald, J. Shan and K. F. Mak, *Nature Nanotechnology*, 2024, **19**, 28–33.
21 W. Zhao, K. Kang, L. Li, C. Tschirhart, E. Redekop, K. Watanabe, T. Taniguchi, A. Young, J. Shan and K. F. Mak, 2022.
22 T. Li, S. Jiang, B. Shen, Y. Zhang, L. Li, Z. Tao, T. Devakul, K. Watanabe, T. Taniguchi, L. Fu, J. Shan and K. F. Mak, *Nature*, 2021, **600**, 641–646.
23 C. Nayak, S. H. Simon, A. Stern, M. Freedman and S. Das Sarma, *Rev. Mod. Phys.*, 2008, **80**, 1083–1159.
24 T. T. Pham, R. Castelino, A. Felten and R. Sporken, *Applied Surface Science*, 2020, **523**, 146428.
25 Y. Huang, Y.-H. Pan, R. Yang, L.-H. Bao, L. Meng, H.-L. Luo, Y.-Q. Cai, G.-D. Liu, W.-J. Zhao, Z. Zhou, L.-M. Wu, Z.-L. Zhu, M. Huang, L.-W. Liu, L. Liu, P. Cheng, K.-H. Wu, S.-B. Tian, C.-Z. Gu, Y.-G. Shi, Y.-F. Guo, Z. G. Cheng, J.-P. Hu, L. Zhao, G.-H. Yang, E. Sutter, P. Sutter, Y.-L. Wang, W. Ji, X.-J. Zhou and H.-J. Gao, *Nature Communications*, 2020, **11**, 2453.
26 Y. Zhang, M. M. Ugeda, C. Jin, S.-F. Shi, A. J. Bradley, A. Martín-Recio, H. Ryu, J. Kim, S. Tang, Y. Kim, B. Zhou, C. Hwang, Y. Chen, F. Wang, M. F. Crommie, Z. Hussain, Z.-X. Shen and S.-K. Mo, *Nano Letters*, 2016, **16**, 2485–2491.
27 G. Liu, G. Wang, Y. Zhu, H. Zhang, G. Zhang, X. Wang, Y. Zhou, W. Zhang, H. Liu, L. Zhao, J. Meng, X. Dong, C. Chen, Z. Xu and X. J. Zhou, *Review of Scientific Instruments*, 2008, **79**, year.
28 P. E. Blöchl, *Phys. Rev. B*, 1994, **50**, 17953–17979.
29 G. Kresse and D. Joubert, *Phys. Rev. B*, 1999, **59**, 1758–1775.
30 G. Kresse and J. Furthmüller, *Computational materials science*, 1996, **6**, 15–50.
31 G. Kresse and J. Furthmüller, *Physical review B*, 1996, **54**, 11169.
32 K. Lee, É. D. Murray, L. Kong, B. I. Lundqvist and D. C. Langreth, *Physical Review B*, 2010, **82**, 081101.
33 M. Dion, H. Rydberg, E. Schröder, D. C. Langreth and B. I. Lundqvist, *Physical review letters*, 2004, **92**, 246401.
34 J. Klimeš, D. R. Bowler and A. Michaelides, *Physical Review B*, 2011, **83**, 195131.
35 J. Hong, Z. Hu, M. Probert, K. Li, D. Lv, X. Yang, L. Gu, N. Mao, Q. Feng, L. Xie *et al.*, *Nature communications*, 2015, **6**, 6293.
36 J. Qiao, X. Kong, Z.-X. Hu, F. Yang and W. Ji, *Nature communications*, 2014, **5**, 4475.

View Article Online
DOI: 10.1039/D4NR05191B

37 J. Qiao, Y. Pan, F. Yang, C. Wang, Y. Chai and W. Ji, *Science bulletin*, 2018, **63**, 159–168.

38 Z.-X. Hu, X. Kong, J. Qiao, B. Normand and W. Ji, *Nanoscale*, 2016, **8**, 2740–2750.

39 Y. Zhao, J. Qiao, P. Yu, Z. Hu, Z. Lin, S. P. Lau, Z. Liu, W. Ji and Y. Chai, *Advanced Materials (Deerfield Beach, Fla.)*, 2016, **28**, 2399–2407.

40 Y. Zhao, J. Qiao, Z. Yu, P. Yu, K. Xu, S. P. Lau, W. Zhou, Z. Liu, X. Wang, W. Ji *et al.*, *Advanced Materials*, 2017, **29**, 1604230.

41 J. P. Perdew, K. Burke and M. Ernzerhof, *Physical review letters*, 1996, **77**, 3865.

42 C. Ruppert, B. Aslan and T. F. Heinz, *Nano Letters*, 2014, **14**, 6231–6236.

43 See Supplemental Material at http:// *** for the details.

44 T. Böker, R. Severin, A. Müller, C. Janowitz, R. Manzke, D. Voß, P. Krüger, A. Mazur and J. Pollmann, *Physical Review B*, 2001, **64**, 235305.

45 Y. Zhang, T.-R. Chang, B. Zhou, Y.-T. Cui, H. Yan, Z. Liu, F. Schmitt, J. Lee, R. Moore, Y. Chen, H. Lin, H.-T. Jeng, S.-K. Mo, Z. Hussain, A. Bansil and Z.-X. Shen, *Nature Nanotechnology*, 2014, **9**, 111–115.

46 J. A. Miwa, S. Ulstrup, S. G. Sørensen, M. Dendzik, A. G. Čabo, M. Bianchi, J. V. Lauritsen and P. Hofmann, *Physical review letters*, 2015, **114**, 046802.

47 M. Dendzik, M. Michiardi, C. Sanders, M. Bianchi, J. A. Miwa, S. S. Grønborg, J. V. Lauritsen, A. Bruix, B. Hammer and P. Hofmann, *Physical Review B*, 2015, **92**, 245442.

48 T. T. Han, L. Chen, C. Cai, Z. G. Wang, Y. D. Wang, Z. M. Xin and Y. Zhang, *Phys. Rev. Lett.*, 2021, **126**, 106602.

49 C. Robert, R. Picard, D. Lagarde, G. Wang, J. P. Echeverry, F. Cadiz, P. Renucci, A. Högele, T. Amand, X. Marie, I. C. Gerber and B. Urbaszek, *Physical Review B*, 2016, **94**, 155425.

50 N. Zibouche, A. Kuc, J. Musfeldt and T. Heine, *Annalen der Physik*, 2014, **526**, 395–401.

51 I. G. Lezama, A. Arora, A. Ubaldini, C. Barreteau, E. Giannini, M. Potemski and A. F. Morpurgo, *Nano Letters*, 2015, **15**, 2336–2342.

52 S. Helmrich, R. Schneider, A. W. Achtstein, A. Arora, B. Herzog, S. M. de Vasconcellos, M. Kolarczik, O. Schöps, R. Bratschitsch, U. Woggon and N. Owschimikow, *2D Materials*, 2018, **5**, 045007.

53 M. Kang, B. Kim, S. H. Ryu, S. W. Jung, J. Kim, L. Moreschini, C. Jozwiak, E. Rotenberg, A. Bostwick and K. S. Kim, *Nano Letters*, 2017, **17**, 1610–1615.

54 S. B. Desai, G. Seol, J. S. Kang, H. Fang, C. Battaglia, R. Kapadia, J. W. Ager, J. Guo and A. Javey, *Nano Letters*, 2014, **14**, 4592–4597.

55 W. Jin, P.-C. Yeh, N. Zaki, D. Zhang, J. T. Sadowski, A. Al-Mahboob, A. M. van der Zande, D. A. Chenet, J. I. Dadap, I. P. Herman, P. Sutter, J. Hone and R. M. Osgood, *Physical Review Letters*, 2013, **111**, 106801.

56 H. Yuan, Z. Liu, G. Xu, B. Zhou, S. Wu, D. Dumcenco, K. Yan, Y. Zhang, S.-K. Mo, P. Dudin, V. Kandyba, M. Yablonskikh, A. Barinov, Z. Shen, S. Zhang, Y. Huang, X. Xu, Z. Hussain, H. Y. Hwang, Y. Cui and Y. Chen, *Nano Letters*, 2016, **16**, 4738–4745.

57 W. Zhao, Z. Ghorannevis, L. Chu, M. Toh, C. Kloc, P.-H. Tan and G. Eda, *ACS Nano*, 2013, **7**, 791–797.

58 J. Kutrowska-Girzycka, E. Zieba-Ostój, D. Biegańska, M. Florian, A. Steinhoff, E. Rogowicz, P. Mrowiński, K. Watanabe, T. Taniguchi, C. Gies, S. Tongay, C. Schneider and M. Syperek, *Applied Physics Reviews*, 2022, **9**, year.

59 B. Han, J. M. Fitzgerald, L. Lackner, R. Rosati, M. Esmann, F. Eilenberger, T. Taniguchi, K. Watanabe, M. Syperek, E. Malic and C. Schneider, *Physical Review Letters*, 2025, **134**, 076902.

60 I. V. Lebedeva, A. S. Minkin, A. M. Popov and A. A. Knizhnik, *Physica E: Low-dimensional Systems and Nanostructures*, 2019, **108**, 326–338.

61 A. H. Reshak and M. Jamal, *Journal of Alloys and Compounds*, 2012, **543**, 147–151.

62 K. F. Mak, C. Lee, J. Hone, J. Shan and T. F. Heinz, *Physical Review Letters*, 2010, **105**, 136805.

63 G. Froehlicher, E. Lorchat and S. Berciaud, *Physical Review B*, 2016, **94**, 085429.

64 J. M. Riley, F. Mazzola, M. Dendzik, M. Michiardi, T. Takayama, L. Bawden, C. Granerød, M. Leandersson, T. Balasubramanian, M. Hoesch, T. K. Kim, H. Takagi, W. Meevasana, P. Hofmann, M. S. Bahramy, J. W. Wells and P. D. C. King, *Nature Physics*, 2014, **10**, 835–839.

65 Y. Zhang, H. Li, H. Wang, R. Liu, S.-L. Zhang and Z.-J. Qiu, *ACS Nano*, 2015, **9**, 8514–8519.

66 K. F. Mak, K. He, J. Shan and T. F. Heinz, *Nature Nanotechnology*, 2012, **7**, 494–498.

67 P. Eickholt, C. Sanders, M. Dendzik, L. Bignardi, D. Lizzit, S. Lizzit, A. Bruix, P. Hofmann and M. Donath, *Physical Review Letters*, 2018, **121**, 136402.

68 S. Mahatha and K. S. Menon, *Journal of Electron Spectroscopy and Related Phenomena*, 2014, **193**, 43–47.

69 A. Bruix, J. A. Miwa, N. Hauptmann, D. Wegner, S. Ulstrup, S. S. Grønborg, C. E. Sanders, M. Dendzik, A. Grubišić Čabo, M. Bianchi, J. V. Lauritsen, A. A. Khajetoorians, B. Hammer and P. Hofmann, *Phys. Rev. B*, 2016, **93**, 165422.

View Article Online
DOI: 10.1039/D4NR05191B

Data availability statements

The data supporting this article have been included as part of the Supplementary Information.